Fast Light Curve Inversion for Regular and Tumbling Attitude Motion

Alexander Burton, Carolin Frueh
School of Aeronautics and Astronautics, Purdue University

ABSTRACT

When a resolved image of an object cannot be taken, its light curve can still be used to obtain information about its albedo-shape, including material composition, and attitude through the process of light curve inversion. However, even when the object's shape is known, attitude estimation is plagued by ambiguities and non-convergence errors. Convergence errors often arise due to an insufficiently good first guess or motion constraints. This paper offers a robust attitude estimation method for any torque-free rotational motion with no restrictions on the moments of inertia to address these problems. Possible orientations matching a specific brightness measurement are found to generate initial attitude guesses. Then, a swarm optimizer finds multiple attitude time histories that match the input light curve. Fully analytic torque-free expressions are used to compute propagated attitudes quickly. For non-convex objects, an approximation of the reflection model is used. Finally, the best-fitting attitude time history estimates are refined using a quasi-Newton method. The method is demonstrated using noiseless simulated light curves for a simple tetrahedron and a complex satellite model with several thousand surface elements.

1. INTRODUCTION

When an object in space is too far away for a resolved image to be taken, characterizing it via brightness measurements over time is still possible. These brightness measurements, also called the light curve, contain information about the object's shape, material properties, and attitude, among other factors. The process of recovering information from a light curve is known as light curve inversion. In this study, the specific problem of recovering attitude information from the light curve of an artificial space object is considered. The use case is a known space debris object, a spacecraft that has lost contact with its operators, or a similar situation where an object's shape is known but not its attitude. Specifically, the object's shape and the albedo-area of each surface are assumed to be known, as well as its orbit from astrometric measurements.

Solutions to the light curve inversion problem for attitude estimation, or the attitude inversion problem, face two difficulties. The first is convergence. Because the attitude inversion problem is nonlinear, initial guesses for the object's attitude and angular velocity are required. Such a guess may not be available in all cases, especially for debris or a tumbling satellite. However, many attitude estimation methods can only converge to the correct solution with a sufficiently good initial guess of the object's state, particularly for angular velocity. For example, in Wetterer and Jah [1], attitude inversion using an unscented Kalman filter on simulated measurements only converged to the correct solution if the initial angular velocity guess was within approximately 0.003 rad/s of the truth. The Euler angles describing its attitude were initially within about 52°of their true values. These values illustrate that, while there can be a significant amount of error in the initial attitude guess, the initial angular velocity guess requires more precision. The particle filter by Linares et al. [2] also found a converged solution with initial estimate errors of the same magnitude for both attitude and angular velocity. By contrast, the method proposed in this study performs a broad search of the solution space to autonomously generate initial state guesses without any input from the operator.

The second difficulty is the ambiguity of brightness measurements. As discussed by Gagnon and Crassidis [3] for two-dimensional objects and Burton and Frueh [4, 5] for three-dimensional objects, any given brightness measurement could correspond to many different object attitudes. This ambiguity is present even when an object's shape, reflective properties, and position are perfectly known, and there is no measurement noise. This ambiguity also holds for an entire light curve [2, 6]. Two or more distinct attitude time histories can match a specific set of brightness measurements equally well. In the absence of a priori information about the observed object's attitude, this ambiguity must be taken into account.

As a result of the problem's ambiguity, some approaches to attitude inversion limit their scope. Some of these do not attempt to estimate attitude directly, but only the type of motion undergone by an object [7, 8]. Other methods may be limited to specific shapes or types of motion [9, 10]. Alternatively, others have used solvers such as the particle filter [2] or adaptive Gaussian filter [6] that can capture the multimodal nature of the attitude estimate's probability distribution. These solvers are capable of addressing the ambiguity of the problem but still require an initial guess, and in the cited papers, are only tested on objects rotating about a single axis [2, 6], which is not generally realistic for objects in Earth orbit [7, 11].

The method proposed in this study addresses the ambiguity difficulty without reducing the problem's scope and without assuming prior knowledge of the object's attitude or angular velocity. A pair of particle swarm optimizers (PSOs) are used to generate initial attitude and state guesses for the object of interest based on the light curve measurements. Some of these initial guesses or estimates are then passed to a quasi-Newton optimizer [12] to be further refined. No assumption is made about the object of interest's motion apart from its being approximately torque-free. The light curve's ambiguity is addressed by generating multiple attitude estimates, which can be compared with each other and, if necessary, ruled out using follow-up observations.

This paper begins by discussing the PSOs used to solve the attitude inversion problem. It then describes the analytic attitude solutions and the reason for their adoption. Finally, the method is applied to three test cases involving rapid torque-free rotation. In each case, the object begins with an angular velocity of 1.5 rad/s about a random axis, and the light curve consists of twenty-five noiseless measurements taken over twenty seconds. The first test case is a convex object with axisymmetric moments of inertia (MOI). The second is the same object with non-symmetric MOI, and the third case is a detailed model of the Transiting Exoplanet Survey Satellite (TESS) [13] following the same attitude trajectory.

2. INITIAL ATTITUDE PARTICLE SWARM OPTIMIZER

2.1 Overview

The particle swarm optimizer (PSO) proposed by Eberhart and Kennedy [14] uses the social behavior of animals moving in a swarm or flock as a model for searching the solution space of an optimization problem. Two PSOs are used in this study. The first is used to find possible orientations of an observed object at the initial measurement time, and the second is used to perform the light curve inversion. This section and Section 3 will each show how a PSO was applied to the specific problems of finding possible initial attitudes and estimating attitude time histories.

2.2 Cost Function

Let $J(\boldsymbol{x})$ be the cost function of an optimization problem. A "particle" is then a possible solution to the optimization problem described using the estimated state vector $\hat{\boldsymbol{x}}_i$ and a velocity vector $\boldsymbol{v}_i$ where i is the particle's index. For the possible initial attitude PSO, the cost function $J = J_{att}$ is:

$$J_{att} = \frac{I_m - I_L(\hat{\boldsymbol{q}})}{I_m} \tag{1}$$

where I_m is the measured light curve intensity at the initial time step, I_L is the simulated intensity for a given attitude, and $\hat{\boldsymbol{q}} = (s, \boldsymbol{v})$ is a quaternion composed of a scalar s and vector $\boldsymbol{v}$. The quaternion $\hat{\boldsymbol{q}}$ corresponds to the estimated rotation from an approximately inertial space-fixed coordinate frame to a body-fixed frame in the object of interest.

The particles move through the problem's solution space, searching for the minima of the cost function. Generally, the particles are informed by what other swarm members have seen, making it more likely that they will converge on a single global minimum rather than settling into many local minima.

2.3 Initial Particle Creation

At the PSO's start, each particle's initial position $\hat{\boldsymbol{x}}_i$ must be set. The positions may be set randomly, as suggested by Eberhart and Kennedy [14], evenly distributed across the solution space, or placed at pre-selected points.

The solution space for the possible initial attitude PSO is the set of unit quaternions. The four-dimensional unit quaternions are represented using four-dimensional spherical coordinates $\varepsilon, \zeta, \eta \in [-\pi, \pi]$ to allow the motion of particles in the solution space to be unconstrained.

$$\hat{\boldsymbol{q}} = (q_0, \boldsymbol{q}_v) = \left(\sin\varepsilon \sin\zeta \sin\eta, \begin{bmatrix} \cos\varepsilon \\ \sin\varepsilon \cos\zeta \\ \sin\varepsilon \sin\zeta \cos\eta \end{bmatrix} \right) \tag{2}$$

The particles are initialized as evenly spaced in attitude space with spherical coordinates $\hat{\boldsymbol{x}}_i$. Each particle is also assigned a random initial velocity $\boldsymbol{v}_i$ in the solution space.

$$\hat{\boldsymbol{x}}_i = \begin{bmatrix} \varepsilon_i \\ \zeta_i \\ \eta_i \end{bmatrix} \qquad\qquad \boldsymbol{v}_i = \begin{bmatrix} v_{i,\varepsilon} \\ v_{i,\zeta} \\ v_{i,\eta} \end{bmatrix} \tag{3}$$

The initialization process is completed by evaluating the cost function J at each particle's location $\hat{\boldsymbol{x}}_i$. Each particle stores its current position and the corresponding cost as the best solution $\hat{\boldsymbol{x}}_{B,i}$ it has seen with cost $J_{B,i}$.

The PSO may also allow particles to communicate with each other. If this is the case, then each particle is assigned other particles as "neighbors" and records the lowest-cost solution among it and its neighbors as the local best $\hat{\boldsymbol{x}}_{l,i}$ with cost $J_{l,i}$. The best solution seen by any particle in the swarm may also be recorded as the globally best solution $\hat{\boldsymbol{x}}_g$ with cost J_g.

2.4 Iterations

After initializing the PSO, the particles are moved through solution space a set number of times to look for the minima of $J(\hat{\boldsymbol{x}})$. Before moving the particles, their velocities are updated based on the best solutions found so far. Each particle is accelerated by a random amount according to the following expression:

$$\boldsymbol{v}_i^+ = \boldsymbol{v}_i^- + \alpha \left[R_b(\hat{\boldsymbol{x}}_{B,i} - \hat{\boldsymbol{x}}_i) + w_l R_l(\hat{\boldsymbol{x}}_{l,i} - \hat{\boldsymbol{x}}_i) + w_g R_g(\hat{\boldsymbol{x}}_g - \hat{\boldsymbol{x}}_i) \right], \tag{4}$$

where $\boldsymbol{v}_i^{-/+}$ is the velocity of the i-th particle before and after the update, α is a positive constant, and the R_x terms are random numbers between 0 and 1. The non-negative weights w_l and w_g control how much importance the PSO gives to the local best and globally best solutions, respectively. The magnitude of $\boldsymbol{v}_i^+$ is capped at a set value v_{max}.

For the initial attitude PSO, w_l and w_g are set to zero. These weights force each particle to consider only the best solutions it has personally encountered, meaning that the PSO will find a larger number of local minima than if the particles communicated with each other. In many contexts, this would not be desirable behavior. However, the possible attitude PSO aims to locate as many attitudes as possible, so particles settling into many local minima is desirable in this context.

Once the particle velocities have been updated, the particles are moved through the solution space as shown below:

$$\hat{\boldsymbol{x}}_i^+ = \hat{\boldsymbol{x}}_i^- + \boldsymbol{v}_i^+ \tag{5}$$

where $\hat{\boldsymbol{x}}_i^{-/+}$ is the position of the i-th particle before and after being updated.

After this step, the cost function $J(\boldsymbol{x})$ is evaluated at each particle's new location. The particles' personal and local best solutions and the swarm's global best solution are then updated. If the completion criteria have been reached, the PSO outputs the results. If not, the particles are accelerated and moved again per Equation (4) and Equation (5).

2.5 Motion in Angle Space

The definition of the attitude space representation in Equation (2) constrained the spherical coordinates $\{\varepsilon, \zeta, \eta\}$ to be between $-\pi$ and π, but Equation (5) allows unconstrained movement of the particles through solution space. Therefore, the periodic nature of $\hat{\boldsymbol{q}}(\varepsilon, \zeta, \eta)$ in Equation (2) is leveraged to keep the particles within that range.

Let $\xi \in \{\varepsilon, \zeta, \eta\}$ be one of the spherical coordinates. The periodicity of the attitude representation means that changing ξ by $\pm 2\pi$ results in the same attitude representation. The subtraction operation in Equation (4) may therefore be calculated as follows:

$$\xi_{B,i} - \xi_i = \begin{cases} \xi_{B,i} - \xi_i - 2\pi & \text{if } (\xi_{B,i} - \xi_i) > \pi \\ \xi_{B,i} - \xi_i + 2\pi & \text{if } (\xi_{B,i} - \xi_i) < -\pi \\ \xi_{B,i} - \xi_i & \text{otherwise} \end{cases}, \qquad \xi \in \{\varepsilon, \zeta, \eta\}. \tag{6}$$

The addition operation in Equation (5) is also slightly modified. When updating a particle's location, any spherical coordinates that would fall outside the allowed range are shifted by 2π so that they fall inside of it.

$$\xi_i^+ = \begin{cases} \xi_i^- + v_{i,\xi}^+ - 2\pi & \text{if } (\xi_i^- + v_{i,\xi}^+) > \pi \\ \xi_i^- + v_{i,\xi}^+ + 2\pi & \text{if } (\xi_i^- + v_{i,\xi}^+) < -\pi \\ \xi_i^- + v_{i,\xi}^+ & \text{otherwise} \end{cases}, \qquad \xi \in \{\varepsilon, \zeta, \eta\}. \tag{7}$$

3. LIGHT CURVE INVERSION PARTICLE SWARM OPTIMIZER

3.1 State and Cost Function

Once a set of possible attitudes is found at the initial measurement time, another PSO is used to invert the light curve and find initial object states matching the input light curve. The initial object states are the object's attitude and angular velocity at the initial measurement time.

$$\hat{\boldsymbol{x}}_i = \begin{bmatrix} \hat{\boldsymbol{y}}_i \\ \hat{\boldsymbol{\omega}}_i \end{bmatrix} = \begin{bmatrix} \varepsilon_i \\ \zeta_i \\ \eta_i \\ \omega_{i,x} \\ \omega_{i,y} \\ \omega_{i,z} \end{bmatrix} \tag{8}$$

where ε_i, ζ_i, and η_i correspond to the same angles in Equation (3), and $\omega_{i,x}$, $\omega_{i,y}$, and $\omega_{i,z}$ are the components of the object's estimated angular velocity $\hat{\boldsymbol{\omega}}_i$ relative to the space-fixed frame.

The cost function of the light curve inversion PSO is based on how well a propagated light curve matches the input light curve:

$$J_{LC}(\hat{\boldsymbol{y}}_i) = \sum_{j=0}^{N-1} \left[I_{m,j} - I_L(\hat{\boldsymbol{q}}_j) \right]^2, \tag{9}$$

where N is the number of measurements in the input light curve, $I_{m,j}$ is the measured light curve intensity at time t_j, and $\hat{\boldsymbol{q}}_j$ is the attitude at t_j found by propagating the initial state $\hat{\boldsymbol{x}}_i$. Section 4 discusses an analytic attitude propagation method that can be used to calculate $\hat{\boldsymbol{q}}_j$ for torque-free rotational motion.

3.2 Initial Particle Creation

The states in $\hat{\boldsymbol{x}}_i$ are divided into two kinds: the initial attitude states $\hat{\boldsymbol{y}}_i$, and the initial angular velocity states $\hat{\boldsymbol{\omega}}_i$. When initializing the PSO, the attitude and angular velocity states are generated separately, and then a particle is initialized for each attitude-angular-velocity pairing.

The initial attitude states are the possible attitudes found using the possible attitude PSO, and the angular velocity states are randomly generated with a maximum magnitude equal to the Nyquist frequency of the input light curve. Assuming that the light curve measurements are Δt seconds apart, then this maximum magnitude is as follows:

$$\omega_{max} = \frac{\pi}{\Delta t} \text{ rad/s}. \tag{10}$$

Once n initial attitudes $\hat{\boldsymbol{y}}_{(j)}$ and m initial angular velocities $\hat{\boldsymbol{\omega}}_{(j)}$ have been generated, they are combined to form the set of nm initial state guesses.

$$\{\hat{\boldsymbol{x}}_1,\hat{\boldsymbol{x}}_2,...,\hat{\boldsymbol{x}}_m,\hat{\boldsymbol{x}}_{m+1},...,\hat{\boldsymbol{x}}_{nm}\} = \left\{ \begin{bmatrix} \hat{\boldsymbol{y}}_{(1)} \\ \hat{\boldsymbol{\omega}}_{(1)} \end{bmatrix}, \begin{bmatrix} \hat{\boldsymbol{y}}_{(1)} \\ \hat{\boldsymbol{\omega}}_{(2)} \end{bmatrix}, ..., \begin{bmatrix} \hat{\boldsymbol{y}}_{(1)} \\ \hat{\boldsymbol{\omega}}_{(m)} \end{bmatrix}, \begin{bmatrix} \hat{\boldsymbol{y}}_{(2)} \\ \hat{\boldsymbol{\omega}}_{(1)} \end{bmatrix}, ..., \begin{bmatrix} \hat{\boldsymbol{y}}_{(n)} \\ \hat{\boldsymbol{\omega}}_{(m)} \end{bmatrix} \right\} \tag{11}$$

The initial velocities of the particles are then randomly generated. The velocities of each particle in the attitude state space $\boldsymbol{v}_{i,y}$ and angular velocity state space $\boldsymbol{v}_{i,\omega}$ are generated and updated separately.

For the light curve inversion PSO, the local weight w_l and global weight w_g in Equation (4) are not necessarily set to zero. Therefore, particles are assigned neighbors at initialization, which are used to obtain the $\hat{\boldsymbol{x}}_{l,i}$ solutions. Each particle's neighbors are the n_l particles with the same initial attitude estimate $\hat{\boldsymbol{y}}_i$ and the angular velocities closest to $\hat{\boldsymbol{\omega}}_i$.

3.3 Motion in the Solution Spaces

After initialization, the light curve inversion PSO is run as described in Section 2.4. However, because the attitude and angular velocity estimate spaces have different properties, the state components $\hat{\boldsymbol{y}}_i$ and $\hat{\boldsymbol{\omega}}_i$ are updated separately.

The spherical coordinates representing the attitude quaternion are bounded on $[-\pi,\pi]$ just as for the possible attitude PSO. Therefore, the difference between a particle's attitude estimate $\hat{\boldsymbol{y}}_i$ and its the best solutions $\hat{\boldsymbol{y}}_{B/l/g,i}$ is calculated using Equation (6). The position of a particle in attitude space is also updated according to Equation (7) to ensure the spherical coordinates stay in the allowed range.

The angular velocity space is treated as a Cartesian space and updated using Equation (4) and Equation (5). Note that the attitude and angular velocity estimates use different maximum velocities v_{max} and acceleration constants α when updating a particle's velocity in their respective spaces using Equation (4).

4. ANALYTIC TORQUE-FREE MOTION

4.1 Motivation and Attitude Representation

Over the course of a single run, millions of individual attitudes need to be generated by propagating the initial state $\hat{\boldsymbol{x}}_i = \begin{bmatrix} \hat{\boldsymbol{y}}_i & \hat{\boldsymbol{\omega}}_i \end{bmatrix}^T$. This propagation is computationally expensive if done numerically. Therefore, analytic solutions to the torque-free rotational equations of motion are used. Torque-free solutions to the rotational equations of motion have been known for some time but are often not given in full, even in standard textbooks of rigid body dynamics [15]. As such, the torque-free attitude expressions used by the light curve inversion PSO are fully written out in this section.

The version in this study uses a 313 (ϕ,θ,ψ) Euler angle sequence to represent attitude for short axis mode (SAM) rotations and a 131 (ϕ,θ,ψ) Euler angle sequence for long axis mode (LAM) rotations. These sequences were chosen because of the physical meaning of the Euler angles. The first angle ϕ in both sequences is the precession angle, the second angle θ is the nutation angle between the principal rotation axis and the angular momentum vector $\boldsymbol{H}$, and the third angle ψ is the spin angle.

4.2 Short Axis Mode Angular Velocity

Let the body-fixed coordinate system $\hat{b}$ of the object of interest be a principal axis system arranged such that $I_x \leq I_y \leq I_z$, where I_i is the moment of inertia about $\hat{b}_i$. The object is undergoing SAM rotation if it is rotating primarily about the "short" $\hat{b}_z$ axis, and LAM rotation if it is rotating primarily about the "long" $\hat{b}_x$ axis. Mathematically, the two can be distinguished using the dynamic moment of inertia I_d [16]:

$$I_d = \frac{H^2}{2T} \tag{12}$$

where H is the angular momentum magnitude and T is the rotational kinetic energy. If $I_y < I_d$, then the object is experiencing SAM rotation. On the other hand, if $I_d < I_y$, the object is experiencing LAM rotation. If $I_d = I_y$, the object is undergoing a single axis rotation about $\hat{b}_y$.

The analytic expressions for SAM angular velocity are adapted from Benson [16]. The same solution is found in Samarasinha and A'Hearn [17], and similar ones are derived in Thomson [18] and Murakami [19].

$$\omega_x(t) = \pm\omega_e\sqrt{\frac{I_d(I_z-I_d)}{I_x(I_z-I_x)}}\,\mathrm{cn}(\tau,k), \quad \omega_y(t) = \pm\omega_e\sqrt{\frac{I_d(I_z-I_d)}{I_y(I_z-I_y)}}\,\mathrm{sn}(\tau,k), \quad \omega_z(t) = \pm\omega_e\sqrt{\frac{I_d(I_d-I_x)}{I_z(I_z-I_x)}}\,\mathrm{dn}(\tau,k) \tag{13}$$

where $\mathrm{sn}(\tau,k)$, $\mathrm{cn}(\tau,k)$, and $\mathrm{dn}(\tau,k)$ are the Jacobi elliptic functions. The sign of each term is chosen based on the initial angular velocity $\boldsymbol{\omega}(t_0)$. If $\omega_z(t_0) \geq 0$, then all terms use "+." If $\omega_z(t_0) < 0$, then ω_z and either ω_x or ω_y use "−." If $\omega_y(t_0) = 0$, then ω_x is assigned "−"; otherwise, ω_y is assigned "−." The constant ω_e is the effective spin rate

$$\omega_e = \frac{2T}{H}, \tag{14}$$

τ is a timelike parameter, and k is the elliptic modulus. These are all calculated as follows:

$$\tau = n_\tau(t-t_0) + \tau_0 \tag{15}$$

$$n_\tau = \omega_e\sqrt{\frac{I_d(I_d-I_x)(I_z-I_y)}{I_xI_yI_z}} \tag{16}$$

$$\tau_0 = \int_0^\Phi \frac{1}{\sqrt{1-k^2\sin^2 x}}dx = F(\Phi|k^2) \tag{17}$$

$$k^2 = \frac{(I_y-I_x)(I_z-I_d)}{(I_z-I_y)(I_d-I_x)} \tag{18}$$

where $F(\Phi|k^2)$ is the incomplete elliptic integral of the first kind. The angle Φ in Equation (17) is the angle that satisfies the following identities based on the initial angular velocity $\boldsymbol{\omega}(t_0)$:

$$\cos\Phi = \sqrt{\frac{I_x(I_z-I_x)}{I_d(I_z-I_d)}}\frac{\omega_x(t_0)}{\omega_e} \qquad \sin\Phi = \sqrt{\frac{I_y(I_z-I_y)}{I_d(I_z-I_d)}}\frac{\omega_y(t_0)}{\omega_e}. \tag{19}$$

4.3 Short Axis Mode Attitude Solution

The analytic expressions for torque-free SAM rotation follow Murakami [19]. The expressions for the nutation angle $\theta(t)$ and spin angle $\psi(t)$ are found using the definition of the angular momentum vector, given below. Since the Euler angle sequence is defined relative to the angular momentum, the components of the angular momentum unit vector $\hat{h}$ can be written in terms of the Euler angles:

$$\hat{h} = \frac{1}{H}\begin{bmatrix} I_x\omega_x(t) \\ I_y\omega_y(t) \\ I_z\omega_z(t) \end{bmatrix} = \begin{bmatrix} \sin\psi\sin\theta \\ \cos\psi\sin\theta \\ \cos\theta \end{bmatrix}. \tag{20}$$

After some manipulation, expressions for $\theta(t)$ and $\psi(t)$ are found. Note that the nutation angle $\theta(t)$ is limited to the range $[0,\pi]$.

$$\theta(t) = \cos^{-1}\left(\frac{I_z\omega_z(t)}{H}\right) \tag{21}$$

$$\psi(t) = \tan^{-1}\left(\frac{I_x\omega_x(t)}{I_y\omega_y(t)}\right). \tag{22}$$

The precession angle $\phi(t)$ is found using the relation between the Euler angle derivative and the body-frame angular velocity [20]:

$$\dot{\phi} = \frac{1}{\sin\theta}\left(\omega_x \sin\psi + \omega_y \cos\psi\right). \tag{23}$$

After integrating, the solution is found to be:

$$\phi(t) = \frac{H}{I_z}(t-t_0) - \frac{H(I_x-I_z)}{n_\tau I_x I_z}\left[\Pi\left(\mathrm{am}(n_\tau t+\tau_0), -\frac{I_z(I_y-I_x)}{I_x(I_z-I_y)}, k\right) - \Pi\left(\mathrm{am}(\tau_0), \frac{I_z(I_y-I_x)}{I_x(I_z-I_y)}, k\right)\right] \tag{24}$$

where $\mathrm{am}(\tau,k)$ is the Jacobi amplitude function. The constants n_τ, τ_0, and k are defined in Equation (16), Equation (17), and Equation (18), respectively. The Π function is the Jacobi incomplete elliptic integral of the third kind. While Π is useful for the mathematical derivation, the equivalent symmetric elliptic integrals are more convenient when numerically computing the integral [21, 22, 23].

Note that the 313 Euler angles were defined such that the angular momentum unit vector $\hat{h}$ is initially parallel to a space-fixed z-direction unit vector. Therefore, in most cases, an additional rotation will be needed to align the space-fixed frame with the angular momentum unit vector before propagating the Euler angles.

4.4 Long Axis Mode Expressions

An alternate set of angular velocity and attitude equations is used if the object is undergoing LAM rotation. The LAM angular velocity functions [16] are as follows:

$$\omega_x(t) = \pm\omega_e\sqrt{\frac{I_d(I_z-I_d)}{I_x(I_z-I_x)}}\,\mathrm{dn}(\tau,k) \quad \omega_y(t) = \pm\omega_e\sqrt{\frac{I_d(I_d-I_x)}{I_y(I_y-I_x)}}\,\mathrm{sn}(\tau,k), \quad \omega_z(t) = \pm\omega_e\sqrt{\frac{I_d(I_d-I_x)}{I_z(I_z-I_x)}}\,\mathrm{cn}(\tau,k) \tag{25}$$

$$k^2 = \frac{(I_y-I_z)(I_x-I_d)}{(I_y-I_x)(I_z-I_d)} \tag{26}$$

where the sign of each term is chosen based on the initial angular velocity $\boldsymbol{\omega}(t_0)$. If $\omega_x(t_0) > 0$, then all terms use "+." If $\omega_x(t_0) < 0$, then ω_x and either ω_y or ω_z use "−." If $\omega_y(t_0) = 0$, then ω_z is assigned "−"; otherwise, ω_y is assigned "−." The parameter τ is defined as in Equation (15) except that n_τ is

$$n_\tau = \omega_e\sqrt{\frac{I_d(I_z-I_d)(I_y-I_x)}{I_x I_y I_z}} \tag{27}$$

and τ_0 is computed as in Equation (17) with Φ for the LAM case now satisfying the following expressions:

$$\cos\Phi = \sqrt{\frac{I_z(I_z-I_x)}{I_d(I_d-I_x)}}\,\frac{\omega_z(t_0)}{\omega_e} \qquad \sin\Phi = \sqrt{\frac{I_y(I_y-I_x)}{I_d(I_d-I_x)}}\,\frac{\omega_y(t_0)}{\omega_e}. \tag{28}$$

The LAM attitude solution is found in a similar way to the one in Murakami [19]; however, it uses a 131 Euler angle sequence so that ϕ, θ, and ψ are still the precession, nutation, and spin angles, respectively. Because of this change, the expressions are somewhat different. As before, the angular momentum unit vector $\hat{h}$ in the body frame is related to the Euler angles:

$$\hat{h} = \frac{1}{H}\begin{bmatrix} I_x\omega_x(t) \\ I_y\omega_y(t) \\ I_z\omega_z(t) \end{bmatrix} = \begin{bmatrix} \cos\theta \\ -\cos\psi\sin\theta \\ \sin\psi\sin\theta \end{bmatrix}. \tag{29}$$

The nutation angle $\theta(t)$ and spin angle $\psi(t)$ expressions are found directly from Equation (29):

$$\theta(t) = \cos^{-1}\left(\frac{I_x\omega_x(t)}{H}\right) \tag{30}$$

$$\psi(t) = \tan^{-1}\left(\frac{I_z\omega_z(t)}{-I_y\omega_y(t)}\right). \tag{31}$$

In Equation (31), the negative sign is left in the denominator to help determine the spin angle's quadrant. The precession angle ϕ is found by integrating the relationship between the precession rate and the angular velocity components:

$$\dot{\phi} = \frac{1}{\sin\theta}\left(\omega_z\sin\psi - \omega_y\cos\psi\right). \tag{32}$$

After integration, the $\phi(t)$ expression is found:

$$\phi(t) = \frac{H}{I_x}(t-t_0) + \frac{H(I_x-I_z)}{n_\tau I_x I_z}\left[\Pi\left(\text{am}(n_\tau t+\tau_0), -\frac{I_x(I_z-I_y)}{I_z(I_y-I_x)}, k^2\right) - \Pi\left(\text{am}(\tau_0), -\frac{I_x(I_z-I_y)}{I_z(I_y-I_x)}, k^2\right)\right] \tag{33}$$

where k is defined in Equation (26), n_τ is defined in Equation (27), and τ_0 is found with Equation (17) using Φ from Equation (28).

Note that, similar to the SAM case, the 131 Euler angles were defined such that the angular momentum unit vector $\hat{h}$ is initially parallel to a space-fixed x-direction unit vector. Therefore, an additional rotation may be needed to align the space-fixed frame with $\hat{h}$.

4.5 Initial Euler Angles

The Euler angles ϕ, θ, and ψ for both the SAM and LAM cases are computed from the body-frame angular momentum unit vector $\hat{h} = \begin{bmatrix} h_x & h_y & h_z \end{bmatrix}^T$. The initial angles are found using similar expressions in both the SAM and LAM regimes, so they are discussed together. First, the initial nutation angle θ_0 is computed.

$$\theta_0 = \begin{cases} \cos^{-1}(h_x) & \text{if } I_d < I_y \\ \cos^{-1}(h_z) & \text{if } I_d > I_y \\ \pi/2 & \text{if } I_d = I_y \end{cases} \tag{34}$$

Recall that if $I_d = I_y$, the object is undergoing single-axis rotation about the intermediate axis $\hat{b}_y$. Second, the initial spin angle ψ_0 is found.

$$\psi_0 = \begin{cases} \tan^{-1}\left(\frac{h_z/\sin\theta_0}{-h_y/\sin\theta_0}\right) & I_d \le I_y \\ \tan^{-1}\left(\frac{h_x/\sin\theta_0}{h_y/\sin\theta_0}\right) & I_d \ge I_y \end{cases} \tag{35}$$

Both expressions are valid if $I_d = I_y$. Finally, the initial precession angle ϕ_0 is computed.

$$\phi_0 = 4\tan^{-1}\left(\frac{B-\sqrt{A^2+B^2-C^2}}{A+C}\right) \tag{36}$$

where

$$\begin{aligned} A &= (\cos\theta_0+1)\cos\frac{\theta_0}{2}\cos\frac{\psi_0}{2} + \sin\theta_0\sin\frac{\theta_0}{2}\left(\cos\psi_0\cos\frac{\psi_0}{2} + \sin\psi_0\sin\frac{\psi_0}{2}\right) \\ B &= -(\cos\theta_0+1)\cos\frac{\theta_0}{2}\sin\frac{\psi_0}{2} + \sin\theta_0\sin\frac{\theta_0}{2}\left(\cos\psi_0\sin\frac{\psi_0}{2} - \sin\psi_0\cos\frac{\psi_0}{2}\right) \\ C &= \sqrt{2(\cos\theta_0+1)}. \end{aligned} \tag{37}$$

If $A+C=0$, then ϕ_0 is instead

$$\phi_0 = 4\tan^{-1}\left(-\frac{A}{B}\right). \tag{38}$$

5. RESULTS

5.1 Overview

The light curve inversion process is demonstrated on three simulated noiseless light curves. In each case, the object of interest's position, shape, and reflective properties are assumed to be known perfectly. Each light curve consists of twenty-five measurements evenly spaced over a twenty-second interval. Each object is rotating at an initial angular speed $||\hat{\boldsymbol{\omega}}_0||$ of 1.5 rad/s such that there is significant rotation about all three body-frame principle axes. The attitude quaternion $\boldsymbol{q}$ describes the rotation from a body-fixed principle axis system to a system with axes parallel to the Earth-centered inertial coordinate frame.

5.2 Axisymmetric Tetrahedron

As described above, the first light curve is generated by the regular tetrahedron shown in Figure 1. The tetrahedron has diffusely-reflecting sides [24], and each side has a different diffuse reflection coefficient to introduce some asymmetry: 0.1, 0.4, 0.6, and 0.9.

The tetrahedron has axisymmetric moments of inertia with $I_x = I_y = 1$ kg m^2 and $I_z = 1.5$ kg m^2. Initially, it is at a randomly generated attitude $\boldsymbol{q}_0$ rotating at an angular velocity $\boldsymbol{\omega}_0$.

$$\boldsymbol{q}_0 = \left(0.5251, \begin{bmatrix}0.5801\\0.6106\\0.1221\end{bmatrix}\right) \qquad \boldsymbol{\omega}_0 = \begin{bmatrix}0.9174\\0.9564\\0.7027\end{bmatrix} \text{ rad/s} \tag{39}$$

The initial attitude and orientation were propagated for twenty seconds, and twenty-five measurements were taken at evenly-spaced intervals, as shown in Figure 1. Using this set of measurements means that, per Equation (10), the maximum angular speed ω_{max} that can be recovered from the light curve is 3.7699 rad/s, compared to the initial angular velocity magnitude of $||\boldsymbol{\omega}_0|| = 1.5$ rad/s.

The possible attitude PSO was used to locate attitudes that could correspond to the first measurement. The PSO located 201 attitudes $\hat{\boldsymbol{q}}_0$ with corresponding intensity $I_L(\hat{\boldsymbol{q}}_0)$ within 0.1% of the measured $I_{m,0}$ after being run for ten iterations with a population of $10,648$ particles.

The light curve inversion PSO was then run for 125 iterations with a population of 30,150 particles, or 150 angular velocity $\hat{\boldsymbol{\omega}}_0$ guesses per attitude guess $\hat{\boldsymbol{q}}_0$. The top 250 solutions found by the optimizer were then refined using a quasi-Newton algorithm [12]. The attitude time histories are then ranked on how well they match the light curve measurements using the cost function in Equation (9). Despite simulating over three million light curves with twenty-five measurements each, the inversion process took less than two hours on a personal laptop. The majority of that time was spent running the light curve inversion PSO.

Table 1: The errors in the best estimates for the axisymmetric tetrahedron case. The best guess (Estimate 1, bolded) fits the measurements best and is the solver's estimate for the attitude time history; other estimates are included as supplemental information.

		Initial Estimate Error		**Average Estimate Error**	
Rank	Cost J	Attitude [deg]	Ang. Vel. [rad/s]	Attitude [deg]	Ang. Vel. [rad/s]
1	$\mathbf{5.1952 \cdot 10^{-17}}$	$\mathbf{1.45 \cdot 10^{-4}}$	$\mathbf{5.607 \cdot 10^{-7}}$	$\mathbf{1.66 \cdot 10^{-4}}$	$\mathbf{6.231 \cdot 10^{-7}}$
2	$1.1623 \cdot 10^{-16}$	180.00	$1.717 \cdot 10^{-6}$	180.00	$8.310 \cdot 10^{-7}$
3	$3.4778 \cdot 10^{-16}$	180.00	$3.378 \cdot 10^{-6}$	180.00	$1.529 \cdot 10^{-6}$
4	$1.577 \cdot 10^{-15}$	180.00	$6.280 \cdot 10^{-6}$	180.00	$2.955 \cdot 10^{-6}$
5	$2.1987 \cdot 10^{-9}$	5.80	$9.487 \cdot 10^{-4}$	5.76	$2.096 \cdot 10^{-3}$

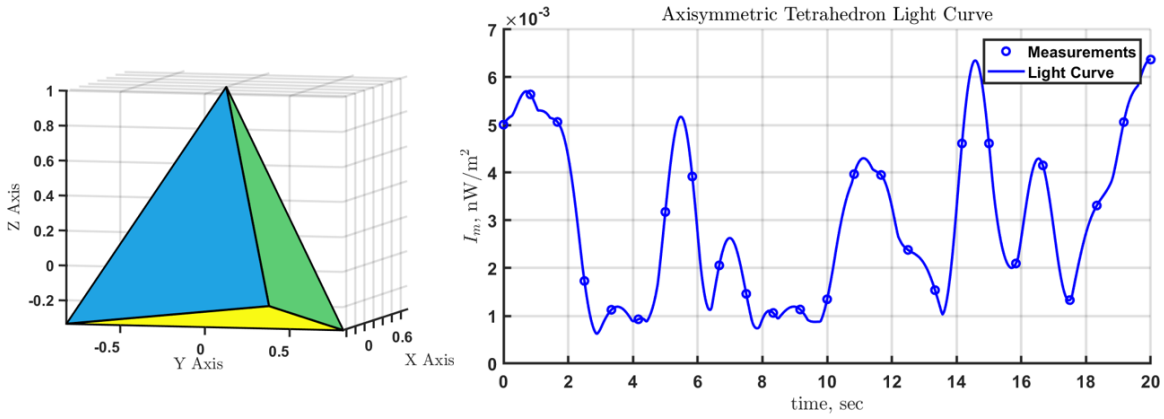

Fig. 1: The light curve and measurements (right) used for estimating the attitude time history of the regular tetrahedron (left). The different colors on the tetrahedron indicate different diffuse reflection coefficients.

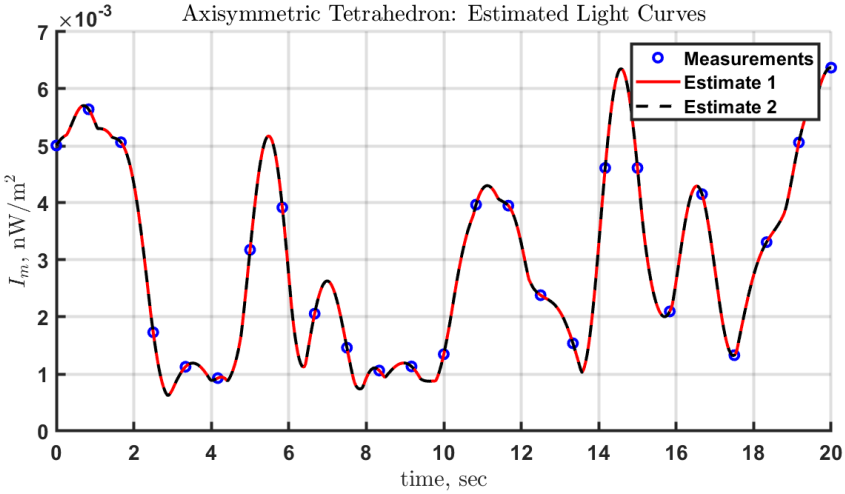

Fig. 2: The light curves corresponding to the best (Estimate 1) and second-best (Estimate 2) attitude time histories produced by the light curve inversion process for the regular tetrahedron.

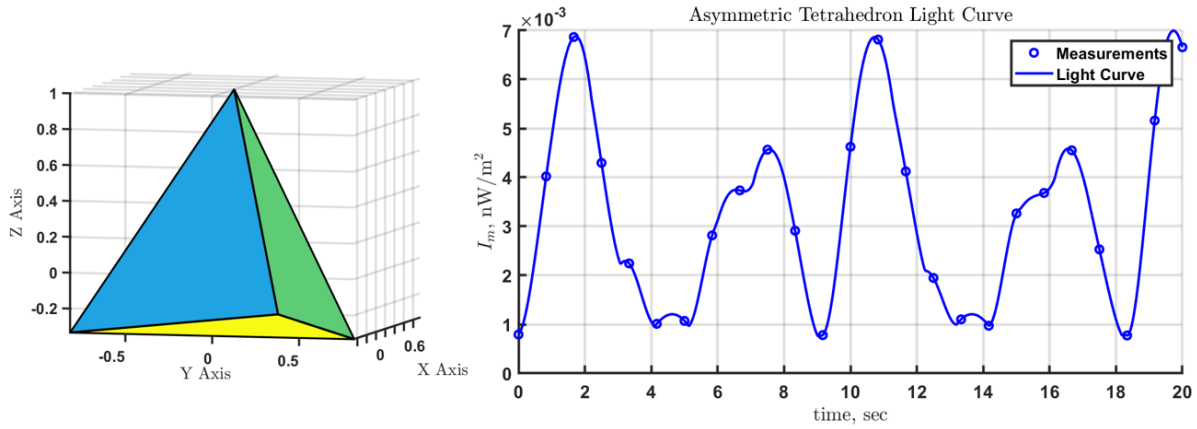

Fig. 3: The light curve and measurements (right) used for estimating the attitude time history of a tetrahedron with asymmetric moments of inertia (left). Visually, the tetrahedron is identical to the one used in the previous case.

The light curves corresponding to the best (Estimate 1) and second-best (Estimate 2) "refined" attitude time history estimates are compared to the measurements in Figure 2. Because it is closest to the measurements, Estimate 1 is chosen by the solver as its solution to the attitude inversion problem. However, additional insight can be gained by examining the other solutions. Visually, the Estimate 1 and Estimate 2 light curves are indistinguishable despite representing attitude time histories with significant differences. According to Table 1, Estimate 1 has an initial attitude estimate error of 0.52 arcseconds, while Estimate 2 is nearly 180°away from the true attitude at all times. The attitude errors are the single-axis rotation angle required to reach the true attitude from the estimate, so Estimate 2 is "flipped" relative to the truth about some axis. However, it still has a low angular velocity estimate error. Indeed, both estimates have a very small average angular velocity error, on the order of 10^{-7} rad/s.

Estimates 3 and 4 are very close to Estimate 2; their initial attitude estimates are both within 3.5 arcseconds of it. Further investigation is needed into why so many attitude estimates are "flipped" in this way. Estimate 5 is an outlier with 5.76°of initial attitude error and relatively high cost J, but the resulting light curve still matches the measurements closely. If complete certainty about the observed object's state is necessary, the accuracy of these estimates to the measurements means that additional a priori information or follow-up measurements would be required to determine which estimate matches the truth most closely.

5.3 Asymmetric Moments of Inertia Tetrahedron

A second case is run using the same regular tetrahedron model as the first but with different moments of inertia and initial states. The tetrahedron no longer has axisymmetric moments of inertia, instead $I_x = 1$ kg m^2, $I_y = 1.5$ kg m^2, and $I_z = 2$ kg m^2. The randomly generated initial orientation $\boldsymbol{q}_0$ and angular velocity $\boldsymbol{\omega}_0$ are as follows:

$$\boldsymbol{q}_0 = \left(0.2866, \begin{bmatrix}0.0573\\0.3535\\0.8886\end{bmatrix}\right) \qquad \boldsymbol{\omega}_0 = \begin{bmatrix}0.8377\\0.2094\\1.2266\end{bmatrix} \text{ rad/s.} \tag{40}$$

This angular velocity is not primarily about any one axis and produces a complex tumbling motion. The light curve corresponding to the initial states in Equation (40) is shown in Figure 3.

The possible attitude PSO was used to find 144 initial attitude guesses, which were then used to initialize the light curve inversion PSO. These initial attitudes were each paired with 150 randomly angular velocity guesses to generate a population of 21,600 particles. The best 250 attitude estimates found after 125 PSO iterations were refined using the quasi-Newton method [12]. Despite having more complex dynamics than the first case, the light curve inversion process for this case was also completed in less than two hours.

The light curves corresponding to the best (Estimate 1) and second-best (Estimate 2) attitude time history estimates are

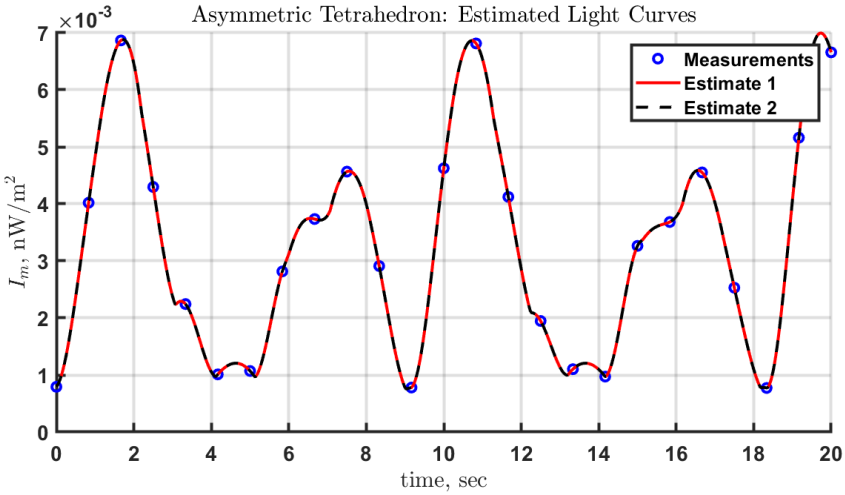

Fig. 4: The light curves corresponding to the best (Estimate 1) and second-best (Estimate 2) attitude time histories produced by the light curve inversion process for the tetrahedron with asymmetric moments of inertia.

Table 2: The errors in the best estimates for the asymmetric tetrahedron case. The best guess (Estimate 1, bolded) fits the measurements best and is the solver's estimate for the attitude time history; other estimates are included as supplemental information.

		Initial Estimate Error		**Average Estimate Error**	
Rank	Cost J	Attitude [deg]	Ang. Vel. [rad/s]	Attitude [deg]	Ang. Vel. [rad/s]
1	$\mathbf{4.3258 \cdot 10^{-16}}$	**180.00**	$\mathbf{8.630 \cdot 10^{-6}}$	**180.00**	$\mathbf{4.466 \cdot 10^{-6}}$
2	$3.4158 \cdot 10^{-15}$	$2.564 \cdot 10^{-3}$	$2.673 \cdot 10^{-5}$	$2.048 \cdot 10^{-3}$	$1.485 \cdot 10^{-5}$
3	$5.8308 \cdot 10^{-12}$	179.90	$1.526 \cdot 10^{-3}$	179.92	$6.423 \cdot 10^{-3}$
4	$1.6356 \cdot 10^{-11}$	179.91	$2.539 \cdot 10^{-3}$	179.95	$1.082 \cdot 10^{-3}$
5	$2.6771 \cdot 10^{-11}$	178.30	$3.189 \cdot 10^{-4}$	178.30	$1.899 \cdot 10^{-4}$

shown in Figure 4. Despite the two estimates having visually indistinguishable light curves, according to Table 2, their two sets of attitudes are rotated almost exactly 180°from each other about some axis; Estimate 2 is another "flipped" attitude estimate with low angular velocity error. Estimates 3 through 5 are variations on Estimate 1. As in the first case, all five estimates fit the measurements so well that follow-up measurements would be required to determine with confidence which one corresponds to the underlying motion of the object.

5.4 TESS Results

For the final case, the light curve is generated using a model of the Transiting Exoplanet Survey Satellite (TESS) [13]. The reflection model is an energy-conserving phong reflection function [25] with a diffuse reflection coefficient of 0.8 and a specular coefficient of 0.2. Figure 5 shows the satellite model and light curve. These light curve measurements are generated using a neural network [26] trained on high-fidelity simulated measurements generated using different attitude and phase angle combinations. This method allows the PSO to model light curve measurements quickly, even for a complex non-convex object.

Since this test aims to demonstrate the effects of an object's geometry and reflective properties on the light curve inversion process, the TESS is modeled as having the same principal moments of inertia as the tetrahedron in the previous section. The initial attitude $\boldsymbol{q}_0$ and angular velocity $\boldsymbol{\omega}_0$ are also those in Equation (40).

The possible attitude PSO was run using the same settings as the tetrahedron case and located 473 possible initial attitudes. These attitudes were each paired with 150 randomly generated initial angular velocity guesses $\hat{\boldsymbol{\omega}}_0$ to initialize the light curve inversion PSO. The second PSO ran for 125 iterations, and the top 250 resulting estimates were refined using a quasi-Newton method [12]. Because of TESS's more complex shape, the inversion process for this case took a little under four hours on a personal laptop, much faster than it would have been if the machine learning approximation

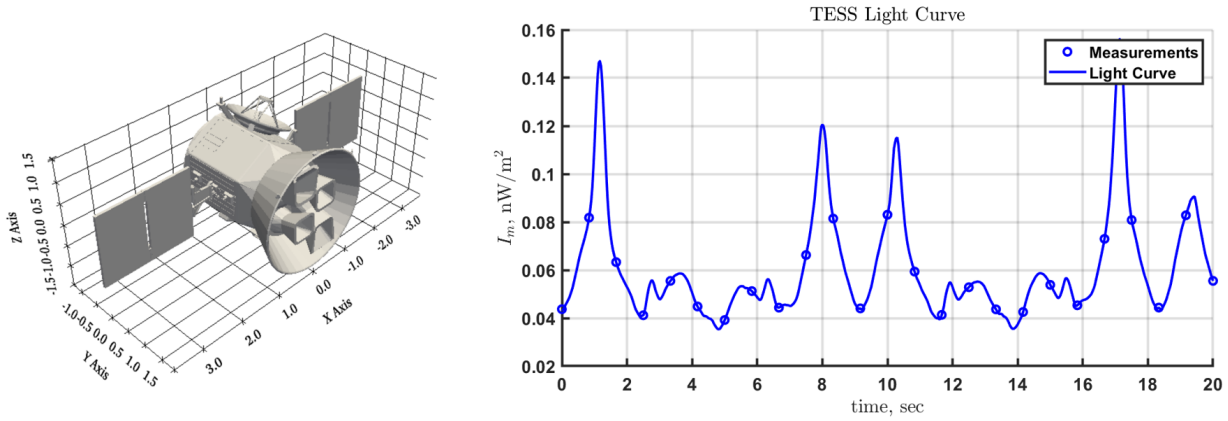

Fig. 5: The TESS model used to simulate the light curve used in the inversion process.

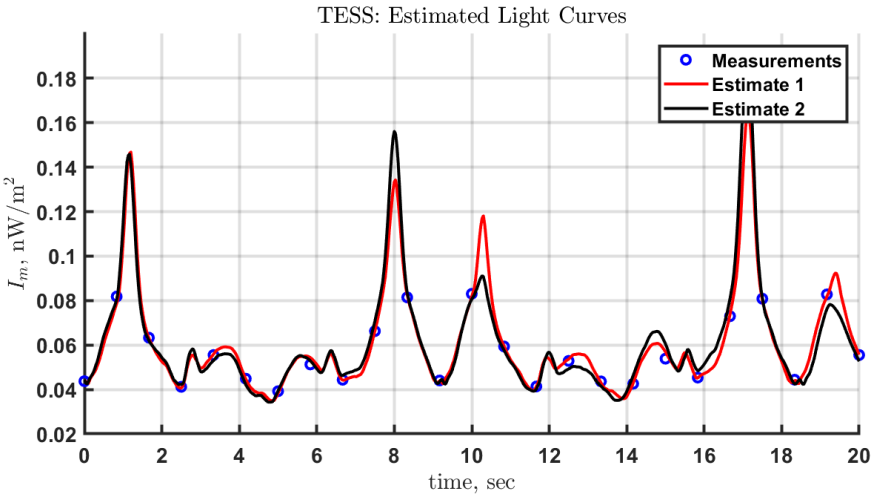

Fig. 6: The light curves corresponding to the best (Estimate 1) and second-best (Estimate 2) attitude time histories produced by the light curve inversion process for TESS.

had not been used for the measurement model.

The light curves corresponding to the best (Estimate 1) and second-best (Estimate 2) attitude time histories according to the cost function in Equation (9) are shown in Figure 6. As before, the solver automatically flags Estimate 1 as the solution to the inversion problem, but additional insight can be gained by examining the other solutions. Unlike the tetrahedron estimated light curves shown in Figure 2 and Figure 4, there is a visible divergence between the estimated light curves in Figure 6. This divergence is likely due to the increased complexity of the non-convex TESS model's brightness function and possibly the measurements' timing. The evenly-spaced measurements did not include information like the height of the specular peaks, which left these prominent features relatively free to vary.

The costs and state estimate errors for the five best solutions found for the TESS case are shown in Table 3. Recall that the attitude errors are the minimum angle for a single-axis rotation between the estimated attitudes and the true attitudes.

Estimates 1 and 4 have initial attitude errors near 180° due to symmetries in the TESS's shape and reflective properties. While an inspection of the model in Figure 5 shows that the satellite is technically asymmetrical due to the presence of small features like the side-mounted antenna, the overall shape is quite symmetrical, which has led to "flipping" the attitude estimate even for resolved-image attitude estimation using the same model [27]. Note that, for Estimate 1, the TESS model has not simply been rotated such that the two solar panels are swapped. Instead, at the initial time step,

Table 3: The errors in the best estimates for the TESS case. The best guess (Estimate 1, bolded) fits the measurements best and is the solver's estimate for the attitude time history; other estimates are included as supplemental information.

		Initial Estimate Error		**Average Estimate Error**	
Rank	Cost J	Attitude [deg]	Ang. Vel. [rad/s]	Attitude [deg]	Ang. Vel. [rad/s]
1	$\mathbf{3.5687 \cdot 10^{-5}}$	**177.23**	**0.05731**	**178.27**	**0.03077**
2	$2.6329 \cdot 10^{-4}$	149.93	0.05957	149.67	0.2082
3	$2.9033 \cdot 10^{-4}$	137.81	0.08076	136.55	0.03659
4	$3.1272 \cdot 10^{-4}$	171.49	2.9695	145.80	2.5886
5	$3.1825 \cdot 10^{-4}$	13.55	0.2379	13.89	0.1668

the $\hat{b}_y$ axis has been rotated 177°, nearly facing the opposite direction as in Figure 5. In contrast, the $\hat{b}_x$ and $\hat{b}_z$ axes only have pointing direction errors of 111°and 69°.

Most of the other top five estimates have attitude errors above 135°, although their angular velocity estimate errors are comparatively low. Estimate 4's higher angular velocity error is due to its initial estimate being almost exactly opposite to $\boldsymbol{\omega}_0$. Only Estimate 5 has an initial attitude error significantly lower, at 13.55°. These results, again, highlight the ambiguity of the light curve inversion results and the need for either follow-up measurements or other tools to determine whether a specific attitude time history corresponds to the actual motion of the observed object. It is also worth noting that the highly nonlinear nature of the attitude inversion problem caused the quasi-Newton algorithm to struggle with the TESS case. The choice of a different algorithm for the final refinement step might significantly improve the fit of the estimated attitude time histories to the light curve.

6. CONCLUSIONS

Space objects too far from an observer for resolved images to be taken can still be characterized using light curve inversion. Existing methods for estimating attitude from a light curve rely on very precise initial state guesses, particularly for angular velocity, to converge on the truth and often do not fully account for the ambiguity of brightness measurements. The presented particle swarm optimizer method addresses these limitations by only assuming that the object's shape, reflective properties, and position are known. It does not require any prior knowledge of its rotational state and is capable of estimating attitude time histories for tumbling objects rotating about three axes simultaneously. Furthermore, the particle swarm considers multiple attitude solutions simultaneously to account for the inherent ambiguity in light curve measurements.

First, a particle swarm optimizer is used to find a set of attitudes that could have produced the first measurement in the light curve. Then, these possible initial attitudes are used to initialize another particle swarm optimizer, which searches the space of initial attitudes and angular velocities to find solutions that could have produced the measured light curve. The best solutions found by this second optimizer are further refined using a quasi-Newton algorithm. Finally, the refined solution that best fits the light curve measurements is autonomously selected as the attitude time history most likely to match the truth. An operator may then inspect the other alternative solutions and decide whether follow-up measurements would be useful for further refining the attitude characterization.

The effectiveness of the inversion process is demonstrated using three test cases. Two cases use a simple diffusely-reflecting tetrahedron with significant rotation about all three principal axes. In the first case, the tetrahedron is modeled as having axisymmetric moments of inertia; in the second case, it is modeled with fully asymmetric inertia. In these two cases, a solution was located within ten arcseconds of the true attitude time history. However, other solutions with a 180°rotation from the true solution were also located that fit the light curve. Even for these "flipped" estimates, the angular velocity estimate was extremely accurate, however. The third case used a detailed non-convex model of the Transiting Exoplanet Survey Satellite. The solution that best fit the light curve for this case was approximately 180°away from the true attitude, though its angular velocity estimate error is still comparatively small. Other solutions that are, on average, between 135°and 150°away from the truth fit the light curve approximately as well as an attitude time history with a 13.89°average attitude error.

These results highlight the ambiguous nature of the attitude inversion problem. Even in the absence of measurement noise and with all other relevant factors known, it is still possible for two or more distinct attitude time histories to

fit an input light curve closely. Selecting a different algorithm for the final refinement step may make distinguishing between these estimates easier. Future work will also apply the particle swarm optimizer method to noisy simulated light curves and real measurements. Finally, the cause of the "flipped" attitude estimates 180°away from the truth will need to be investigated.

7. ACKNOWLEDGMENTS

We are thankful for the support of the Air Force Office of Strategic Research through the grant AFOSR FA9950-19-1-0407. Thanks also to Liam Robinson from the Purdue Space Information Dynamics group for the creation of the Transiting Exoplanet Survey Satellite model and its associated reflection model used to validate the solver.

REFERENCES

[1] Charles J Wetterer and Moriba Jah. Attitude determination from light curves. *Journal of Guidance, Control, and Dynamics*, 32(5):1648–1651, 2009.

[2] Richard Linares, John Crassidis, and Moriba Jah. Particle filtering light curve based attitude estimation for non-resolved space objects. *Advances in the Astronautical Sciences*, 152:119–130, 01 2014.

[3] Stephen R Gagnon and John L Crassidis. Augmenting light curve based attitude estimation with geometric information. In *AIAA SCITECH 2022 Forum*, page 1767, 2022.

[4] Alex Burton and Carolin Frueh. Light curve attitude estimation using the viewing sphere. In *Astrodynamics Specialist Conference 2020*, 2020.

[5] A Burton and C Frueh. Two methods for light curve inversion for space object attitude determination. In *8th European Conference on Space Debris*, 2021.

[6] David Vallverdú Cabrera, Jens Utzmann, and Roger Förstner. The adaptive gaussian mixtures unscented kalman filter for attitude determination using light curves. *Advances in Space Research*, 71(6):2609–2628, 2023.

[7] Conor J Benson, Daniel J Scheeres, William H Ryan, and Eileen V Ryan. Cyclic complex spin state evolution of defunct geo satellites. In *Proceedings of the Advanced Maui Optical and Space Surveillance Technologies Conference, Maui, HI*, 2018.

[8] Jiří Šilha, Jean-Noël Pittet, Michal Hamara, and Thomas Schildknecht. Apparent rotation properties of space debris extracted from photometric measurements. *Advances in space research*, 61(3):844–861, 2018.

[9] JG Williams. The determination of the orientation of a tumbling cylinder from the shape of the light curve. *OFFICE OF AEROSPACE RESEARCH*, page 31, 1967.

[10] Patrick Koller. Attitude determination of cylindrical rocket bodies from optical light curves. University of Bern, 2016. Bachelor Thesis.

[11] Carolin Früh and Moriba K. Jah. Coupled orbit attitude motion of high area-to-mass ratio (hamr) objects including efficient self-shadowing. *Acta Astronautica*, 95:227–241, 2014.

[12] Stephen J Wright. *Numerical optimization*, chapter Quasi-Newton Methods, pages 136–143. 2006.

[13] Keivan G. Stassun, Ryan J. Oelkers, Joshua Pepper, Martin Paegert, Nathan De Lee, Guillermo Torres, David W. Latham, Sté phane Charpinet, Courtney D. Dressing, Daniel Huber, Stephen R. Kane, Sébastien Lépine, Andrew Mann, Philip S. Muirhead, Bárbara Rojas-Ayala, Roberto Silvotti, Scott W. Fleming, Al Levine, and Peter Plavchan. The TESS input catalog and candidate target list. *The Astronomical Journal*, 156(3):102, Aug 2018.

[14] Russell Eberhart and James Kennedy. A new optimizer using particle swarm theory. In *MHS'95. Proceedings of the sixth international symposium on micro machine and human science*, pages 39–43. Ieee, 1995.

[15] Toshio Fukushima. Simple, regular, and efficient numerical integration of rotational motion. *The Astronomical Journal*, 135(6):2298, 2008.

[16] Conor J Benson, Daniel J Scheeres, and Nicholas A Moskovitz. Spin state evolution of asteroid (367943) duende during its 2013 earth flyby. *Icarus*, 340:113518, 2020.

[17] Nalin H Samarasinha and Michael F A'Hearn. Observational and dynamical constraints on the rotation of comet p/halley. *Icarus*, 93(2):194–225, 1991.

[18] WT Thomson. Introduction to space dynamics. *Introduction to space dynamics.. WT Thomson. Dover Publications Inc*, 1986.

[19] Cássio Murakami. Analytical solution of the euler-poinsot problem. *Journal of Geometry and Symmetry in Physics*, 60:25–46, 2021.

[20] James Longuski and Carolin Frueh. Dynamics and vibrations. Lecture Notes, 2019.
[21] B. C. Carlson. Normal elliptic integrals of the first and second kinds. University of North Texas Libraries, UNT Digital Library, May 1963. Last accessed June 8, 2023.
[22] DG Zill and BC Carlson. Symmetric elliptic integrals of the third kind. *Mathematics of computation*, 24(109):199–214, 1970.
[23] Eric W. Weisstein. Carlson elliptic integrals. From *MathWorld*–A Wolfram Web Resource. Last accessed on 6/10/2023. `https://mathworld.wolfram.com/CarlsonEllipticIntegrals.html`.
[24] Carolin Frueh. Space traffic management. Lecture Notes, 2023.
[25] Bernardt Duvenhage, Kadi Bouatouch, and Derrick Kourie. Numerical verification of bidirectional reflectance distribution functions for physical plausibility. In *SAICSIT '13: Proceedings of the South African Institute for Computer Scientists and Information Technologists Conference*, pages 200–208, 10 2013.
[26] F. Pedregosa, G. Varoquaux, A. Gramfort, V. Michel, B. Thirion, O. Grisel, M. Blondel, P. Prettenhofer, R. Weiss, V. Dubourg, J. Vanderplas, A. Passos, D. Cournapeau, M. Brucher, M. Perrot, and E. Duchesnay. Scikit-learn: Machine learning in Python. *Journal of Machine Learning Research*, 12:2825–2830, 2011.
[27] Daigo Kobayashi, Alexander Burton, and Carolin Frueh. Ai-assisted near-field monocular monostatic pose estimation of spacecraft. In *Proceedings of The Advanced Maui Optical and Space Surveillance Technologies (AMOS) Conference*, 09 2023.